PERSPECTIVE

Electrifying Oxide Model Catalysis: Complex Electrodes Based on Atomically-Defined Oxide Films

Olaf Brummel[1] · Jörg Libuda[1]

Abstract

By studying complex model catalysts based on well-defined oxide surfaces, fundamental insights have been obtained into the surface chemistry of many heterogeneously catalyzed processes. In this perspective, we summarize a series of studies, in which we have transferred this model catalysis approach to the field of electrocatalysis. Our model electrocatalysts consisted of Pt nanoparticles (NPs) grown on atomically-defined oxide films. Specifically, we used well-ordered $Co_3O_4(111)$ thin films on an Ir(100) support. The Pt NPs were prepared by physical vapor deposition (PVD) and the particle size was varied from a few nanometers to the sub-nanometer size range. We prepared all model catalysts under ultra-high vacuum (UHV) conditions using a dedicated preparation system. This setup enables us to transfer the model catalysts from UHV into the electrochemical environment to apply various in-situ techniques without exposure to air. We investigated the stability window of pristine $Co_3O_4(111)$ and $Pt/Co_3O_4(111)$ using online inductively coupled plasma mass spectrometry (ICPMS), electrochemical infrared reflection absorption spectroscopy (EC-IRRAS), scanning tunneling microscopy (STM), ex-situ emersion X-ray photoelectron spectroscopy (XPS), and low energy electron diffraction (LEED). Within the stability window (pH 10, 0.3–1.1 V_{RHE}) the surface structure of the model electrocatalysts is preserved. We analyzed identical samples both in UHV and in the electrochemical environment. Specifically, we applied synchrotron radiation photoelectron spectroscopy (SR-PES) and ex-situ emersion XPS to analyze the electronic structure and we used infrared reflection absorption spectroscopy (IRAS), temperature programmed desorption (TPD), EC-IRRAS, and cyclic voltammetry (CV) to study CO adsorption and oxidation. The model electrocatalysts show pronounced particle size effects and metal support interactions are shown to play a key role in their catalytic reactivity. Of particular importance is an interfacial Pt oxide, which is stabilized by the oxide support and exists at electrode potentials as low as 0.5 V_{RHE}. Moreover, spillover effects enable new reaction mechanisms, which involve oxygen from the oxide support. This review demonstrates the potential of the model electrocatalysis approach to provide fundamental insights into complex oxide-based electrocatalysis.

Graphic Abstract
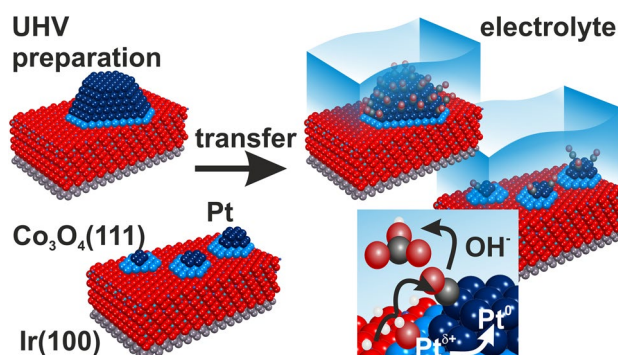
Keywords Electrocatalysis · Nanoparticles · Metal-support interaction · Oxide supports · Spillover · CO oxidation

---

1 Introduction

In the field of heterogeneous catalysis, the model catalysis approach has been contributing substantially to our current understanding of surface chemistry [1–6]. In model catalysis, we use complex but atomically-defined oxide-based catalysts, which bridge the so-called materials gap between single crystal surfaces used in surface science and complex materials used in applied catalysis [7]. A very similar materials gap also exists in electrocatalysis. However, it is fair to say that fundamental understanding in electrocatalysis lags behind the field of heterogeneous catalysis because of the special challenges associated with studying solid/liquid interfaces. Many fundamental insights in electrocatalytic reactions result from studies at single crystal electrodes [8–12]. Here one key step was the development of flame annealing, which enables the use of single crystal electrodes without complex and expensive UHV equipment [13]. Still bridging between single crystal studies and complex electrode materials is difficult in many cases, in particular for complex oxide-based electrodes [14]. Non-surface-science preparation techniques as electrodeposition, chemical vapor deposition, or sputter deposition can help to prepare such complex interfaces, but in most cases, these procedures do not provide true atomic-level-control or they are limited to specific materials.

Oxide-based electrodes are of special interest for a number of reasons. Oxides contribute additional functionalities, e.g. they provide hydroxyl-species, which may increase the electrocatalytic activity [15–22]. Furthermore, oxide supports can stabilize nanoparticles against sintering [23–25].

In the model studies described in this work, we aim transfering the model catalysis approach to electrochemistry, i.e. we 'electrify' well-defined model catalysts by bringing them into the electrochemical environment. Importantly, we use complex atomically defined model systems prepared in UHV, which are characterized by the full portfolio of surface science techniques. There are several challenges associated with this approach. First, we have to develop the methods to transfer the samples in an ultra-clean fashion into the electrochemical environment. Secondly, we have to find appropriate model systems, the structure of which is preserved under electrochemical conditions.

In principle, the combination of surface science preparation and electrochemistry is not new at all [26–28]. Various groups developed related equipment and procedures and used the approach to prepare modified metal surfaces and alloys [27, 29–32]. However, very little work has been done using oxide-based materials. Only in the very last years, first attempts were made to transfer ordered oxide surfaces from UHV into the electrolyte. Müllner et al. studied e.g. the WO_3 adsorption on ordered $TiO_2(110)$ and $Fe_3O_4(001)$ [33] and the stability and catalytic performance of $Fe_3O_4(001)$ and $Fe_3O_4(110)$ during the oxygen evolution reaction (OER) [34]. Fester et al. studied the morphological transformations of CoO_x nanoislands on Au(111) during OER [35]. In this perspective, we summarize the first series of studies from our group following such a surface-science based approach investigating oxide-based electrocatalysis [36–41]. This includes first work in which we studied adsorption and reactivity of noble metal particles on atomically-defined oxide surfaces, which were prepared in UHV and studied both in UHV and in liquid electrolytes under potential control.

2 Coupling UHV Preparation with Electrochemical In-Situ Techniques

First, we address the above-mentioned 'methods challenge'. In the last decades scientists developed a broad range of electrochemical in-situ methods, which are complimentary to classical electrochemical techniques like cyclic voltammetry (CV) [9, 13] and electrochemical impedance spectroscopy (EIS) [42] and which are compatible with well-defined surfaces. Scanning probe microscopy, specifically electrochemical scanning tunneling microscopy (EC-STM) [8, 43, 44] and electrochemical atomic force microscopy (EC-AFM), and diffraction methods like electrochemical surface X-ray diffraction (EC-SXRD) [45] allow us to obtain structural and morphological information. X-ray photoelectron spectroscopy (XPS) [46, 47] addresses the electronic structure of the electrified interface. Volatile products are analyzed by mass spectrometry such as differential electrochemical mass spectrometry (DEMS) [48], online electrochemical mass spectrometry (OLEMS) [49], or electrochemical real-real time mass spectrometry (EC-RTMS) [50]. Vibrational spectroscopy such as electrochemical sum frequency generation (EC-SFG) [51] and electrochemical infrared reflection absorption spectroscopy (EC-IRRAS) [52–54] allows us to analyze adsorbates at the electrode surface. To couple these methods with UHV-prepared model electrocatalysts, it is necessary to set up dedicated preparation chambers, which enable ultra-clean transfer to these in-situ methods. Varieties of different setups were developed in the past, which couple UHV chambers with an electrochemical cell, mainly focusing on the UHV analysis after electrochemical treatment. Several review articles report summaries of the different approaches [26–28, 55, 56]. Most of these setups, however, did not aim at combining UHV preparation with advanced spectroscopic or microscopic in-situ methods. Recently, we described a new UHV preparation system and

transfer system, which is compatible with a broad range of different in-situ methods like e.g. CV, EC-STM, DEMS, and especially EC-IRRAS. Also, we demonstrated the feasibility of the combined experiments [39]. Our setup consists of a conventional UHV chamber and a transfer system (Fig. 1a). For UHV preparation, the main chamber is equipped with the usual preparation tools such as ion gun for Ar^+ sputtering, electron beam evaporators for physical vapor deposition, microbalance for calibration, leak valves for gas exposure, and tools for sample manipulation, heating and cooling (cryostat, filament, k-type thermocouple). For surface characterization, the UHV chamber has an optics for LEED and Auger electron spectroscopy (AES) and a quadrupole mass spectrometer (QMS). The sample is mounted on a sample holder using two rails. This construction enables the release of the sample without any sample holder, thus avoiding contaminations in the electrochemical cell, which may easily result from the sample holder. The transfer system consists of a lock chamber and a glass transfer cell. Gate valves separate the different units. Before transfer, the surface of the sample is saturated with CO. During the transfer, the polished rod of the manipulator, O-rings and a differential pumping stage seal the main chamber from the lock chamber. This allows

purging the lock chamber with inert gas while UHV conditions are preserved in the main chamber. The transfer cell is filled with ultra-pure water purged with an inert gas. A PTFE pin pushes the sample out of the sample holder (see Fig. 1b), which drops into the degassed ultra-pure water. Here it is protected against contamination from the ambient. Finally, the transfer cell is disconnected from the UHV chamber, sealed under inert gas atmosphere, and is transported to the in-situ method of choice. A droplet of ultra-pure water protects the sample surface during the transfer from the transfer cell to the in-situ setup. For post analysis a back transfer of the sample to UHV is possible [39].

3 Characterization of $Co_3O_4(111)$ and Pt/$Co_3O_4(111)$

In the next step, we address the challenge of finding an appropriate model system. A broad range of different epitaxially grown oxide thin films is known [1, 57]. For electrochemical applications, cobalt oxide is particularly interesting as a support. Co_3O_4 itself is highly active for different reactions [58–61], even if the mechanism is poorly understood in

Fig. 1 **a** Schematic representation of the UHV transfer system; **b** sketch of the transfer process from UHV to the electrochemical environment. Adapted with permission from Ref. [37], Copyright 2018, American Chemical Society
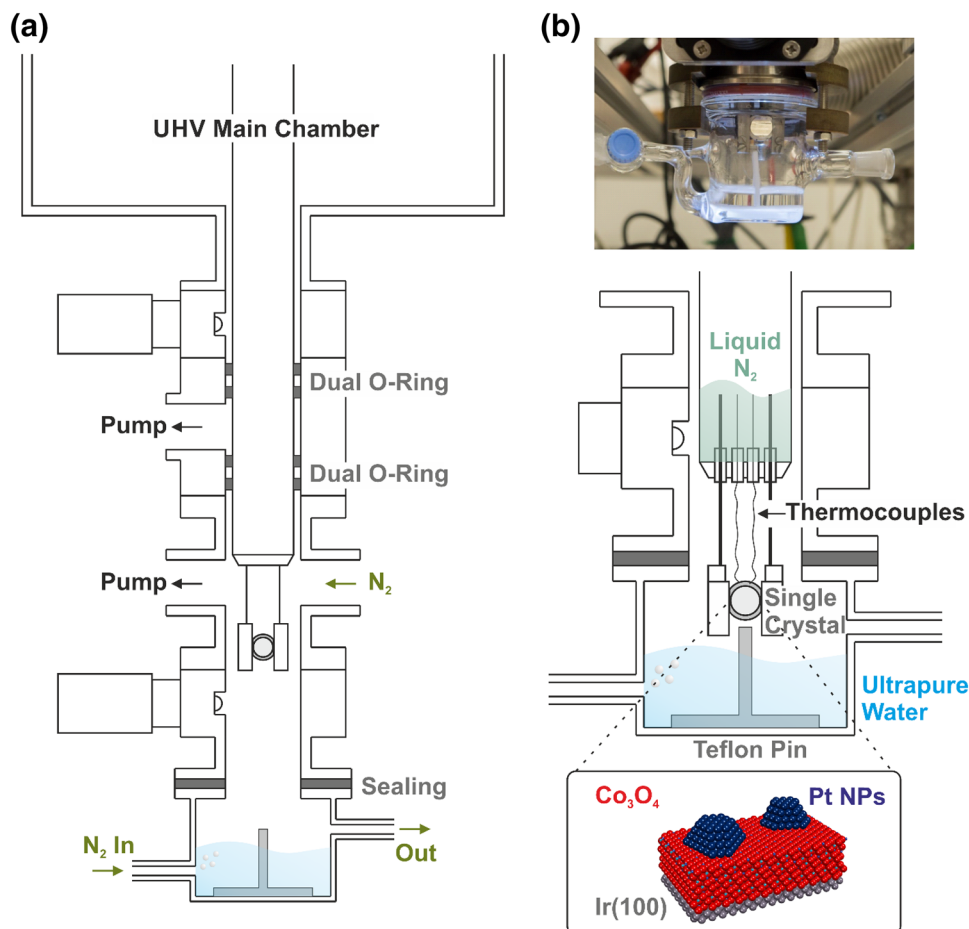
most cases. Co_3O_4 also provides supporting functionalities for noble metal electrocatalysts, for instance for the case of alcohol electrooxidation [20–22].

Highly ordered $Co_3O_4(111)$ films can be prepared on Ir(100) following a recipe developed by Heinz and Hammer (see Fig. 2) [62, 63]. From their LEED I-V and STM studies, the surface structure is known. $Co_3O_4(111)$ grows in a spinel structure and the surface is terminated by a hexagonal layer of tetrahedral Co^{2+} ions with a ion distance of 5.7 Å. The surface has a low defect density as confirmed by STM images (Fig. 2, left) [41]. In our previous work, we investigated $Co_3O_4(111)$ under UHV conditions [64]. To prepare clean and well-defined model electrocatalysts, Pt nanoparticles are grown on the $Co_3O_4(111)$ support by physical vapor deposition (PVD). This approach enables to prepare Pt particle sizes from subnanometer particles with less than 10 atoms per particle to conventional nanoparticles with diameters of ~ 3 nm and ~ 500 Pt atoms per particle, all with a relatively narrow size distribution [41]. We provide an overview over the particle sizes prepared in the reported studies in Table 1 [38].

4 Stability of $Co_3O_4(111)$ and $Pt/Co_3O_4(111)$

For the model electrocatalysis approach, it is not only the surface structure of the initially prepared sample which is important. It is furthermore essential that the surface structure is preserved in the electrochemical environment. The Pourbaix diagram predicts a large thermodynamic stability window for Co_3O_4 in alkaline media [65]. First we studied the electrochemical and dissolution behavior of $Co_3O_4(111)$ by online ICPMS [66, 67] for pH values of 8, 10 and 12 in phosphate buffer [37]. Figure 3 shows Co dissolution rate (upper part) and the corresponding current density (lower part) versus the applied potential, both for the negative (Fig. 3a) and positive (Fig. 3b) limits of the stability window. $Co_3O_4(111)$ has a lower stability at pH

Table 1 Nominal Pt coverage, average NP size, and estimated average number of metal atoms per NP [38]

Nominal Pt coverage (ML)	Average NP size (nm)	Average number of Pt atoms per NP
0.09	< 0.8	< 10
0.14	0.8	~ 10
0.20	0.9	~ 15
0.27	1.0	~ 20
0.45	1.2	~ 30
1.36	2.3	~ 200
2.73	2.9	~ 500

8, while the stability is significant higher for pH 10 and pH 12. The threshold for the onset of dissolution at lower potentials is below 0.3 V_{RHE}. The dissolution is connected to the reduction of the mixed oxide to Co^{2+} species and has a complex kinetics [37]. At pH 8, the dissolution rate in cathodic direction reaches nearly 2000 pg s^{-1} cm^{-2}, while in the reverse scan (data not shown) the dissolution is even higher with 7000 pg s^{-1} cm^{-2}, corresponding to a dissolution rate of ~ 240 ML h^{-1}. Note that we define a monolayer (ML) of cobalt oxide as a single layer of close-packed oxygen with the corresponding layer of Co^{x+} ions. This means that a film of 6 nm thickness dissolves under these conditions in a few minutes. At pH 10 and 12 the dissolution rate is much lower and reaches in cathodic scan direction 60 pg s^{-1} cm^{-2} (2.1 ML h^{-1}) and 30 pg s^{-1} cm^{-2} (1.0 ML h^{-1}) at − 0.3 V_{RHE}, respectively. The corresponding CVs have the most prominent features at pH 12 with reduction peaks at + 0.2 V_{RHE} (C4), − 0.04 V_{RHE} (C5), and − 0.12 V_{RHE} (C6), which we assign to the reduction of Co_3O_4 to $Co(OH)_2$, Co_3O_4 to Co^0, and $Co(OH)_2$ to Co^0, respectively. At pH 10, a reduction feature is present at − 0.25 V_{RHE}, which can be assigned to the reduction of Co_3O_4, $Co(OH)_2$ and/or CoO to Co^0 and pH 8 shows a continuous increase in current [37]. Note that at higher
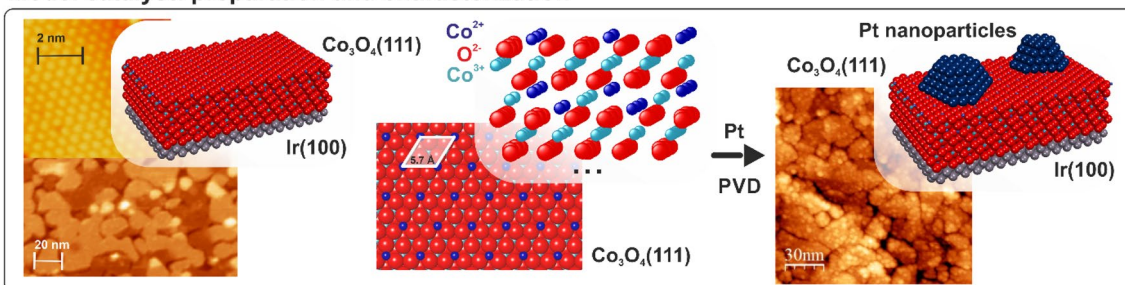

Fig. 2 Preparation and characterization of $Pt/Co_3O_4(111)$ model electrocatalysts; model and STM images of $Co_3O_4(111)$ on Ir(100) (left), crystal and surface structure (middle), and model and STM image of $Pt/Co_3O_4(111)$ (right). Reproduced with permission from Ref. [41], Copyright 2018, Nature Publishing Group
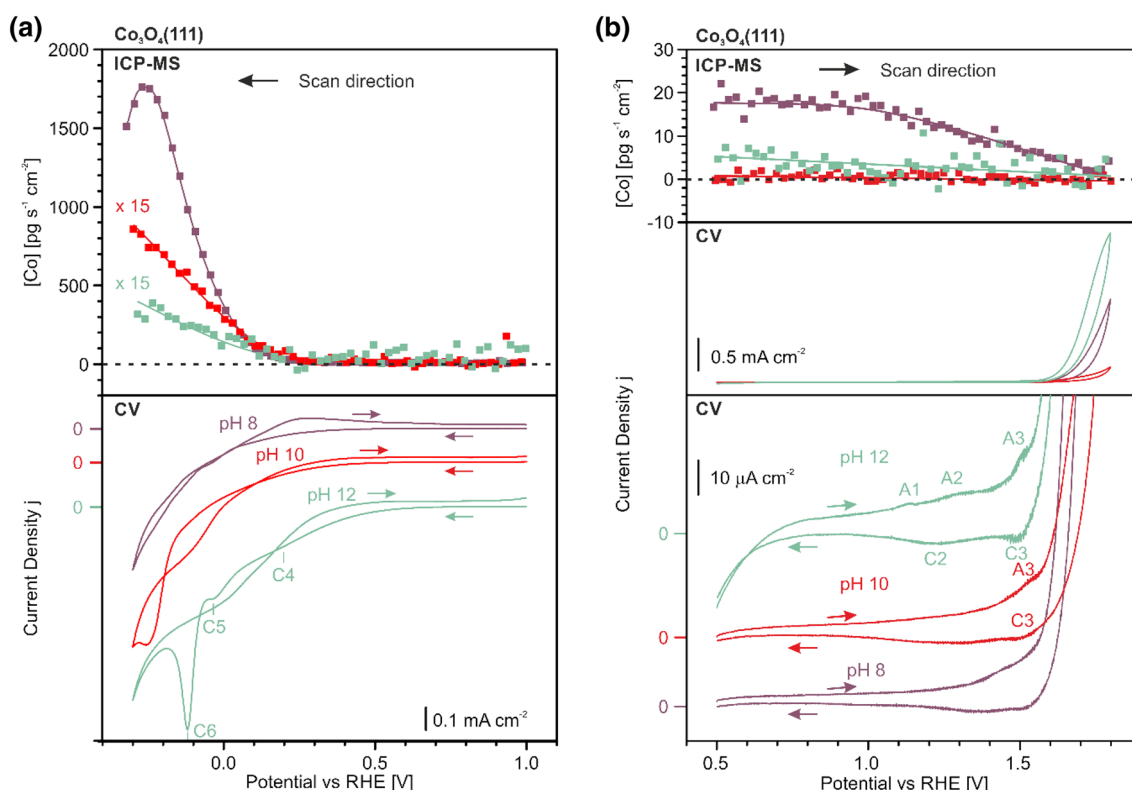
Fig. 3 Electrochemical behavior and dissolution rate of $Co_3O_4(111)/$Ir(100) during potential scan at pH values of pH 8 (purple), pH 10 (red), and pH 12 (green): **a** cathodic scan, **b** anodic scan. All meas- urements were carried out in 0.05 M phosphate buffer with a scan rate of 5 mV s^{-1}. Adapted with permission from Ref. [37], Copyright 2018, American Chemical Society (Color figure online)

pH the formation of $Co(OH)_2$ is favored, while at lower pH CoO is formed.

Much lower Co^{x+} dissolution rates are observed at higher potentials (Fig. 3b, 0.5–1.8 V_{RHE}). While for pH 8, the dis- solution rates of Co^{x+} are up to 20 pg s^{-1} cm^{-2} (0.7 ML h^{-1}), the dissolution at pH 10 and 12 is below the detection limit of the ICPMS (<5 pg s^{-1} cm^{-2}, 0.17 ML h^{-1}) for the whole potential region. In the corresponding CV at pH 12, the most dominant features appear at 1.14 V (A1), 1.31 (A2), and 1.51 V_{RHE} (A3), which were assigned to the oxidation of Co^{2+} surface ions, the formation of a oxyhydroxide layer includ- ing surface reconstruction, and the oxidation of Co(III) to Co(IV) [37]. At lower pH values, the peaks are suppressed, due to the reduced concentration of OH$^-$ ions. From the results, we conclude that the highest stability is obtained at pH 10. At lower pH values, an intensified dissolution is observable and, for higher pH values, redox transformations are more facile in the topmost layer. Therefore, we conclude that the practical stability limits at pH 10 are 0.3 V_{RHE} and 1.3 V_{RHE} with a dissolution of less than 0.2 ML h^{-1} in the potential range between [37].

The stability window was validated by EC-IRRAS, LEED, ex-situ XPS [37, 41], and ex-situ emersion XPS [36, 41]. In Fig. 4, we show selected results before and after

exposure to electrochemical conditions. In the EC-IRRAS experiment, CO was used to probe uncovered parts of the Ir(100) substrate during cycling between 0.3 and 1.3 V_{RHE} for pH values of 5, 8, and 10. At pH 5, the Co_3O_4 film com- pletely dissolves after only 6 cycles. At pH 8, a weak CO_{ads} feature is observable after 8 cycles. At pH 10, no CO adsorp- tion was detectable during the experiment indicating stabil- ity of the oxide film [37]. After the EC-IRRAS experiment, the surface was analyzed by LEED in UHV. Note that we did not introduce any additional cleaning or heating step. While the sample exposed to pH 5 showed LEED pattern of bare Ir(100), at pH 8 we observed a diffuse LEED image indicating complete loss of the long range structure. In sharp contrast, the characteristic LEED pattern of $Co_3O_4(111)$ was preserved at pH 10 (see Fig. 4). This confirms that the long-range structure of the $Co_3O_4(111)$ film is stable under these conditions, even if additional surface hydroxylation and phosphate adsorption occurs in the electrochemical environment [37]. The Co 2p spectrum after preparation of $Co_3O_4(111)$ (Fig. 4a) shows peaks at 779.0 eV for Co^{3+} and 780.2 eV for Co^{2+} and the corresponding satellites at 798.2 and 785.3 eV, respectively. After emersion between 0.5 V_{RHE} (exemplary shown in Fig. 4b) and 1.4 V_{RHE}, the shape of the Co 2p spectrum shows hardly any change as

Fig. 4 Testing the structural and chemical stability of $Co_3O_4(111)$ and $Pt/Co_3O_4(111)$. **a** LEED pattern (144 eV) and XPS (Co 2p) of the freshly prepared $Co_3O_4(111)$ film; STM images (in air) and XPS (Pt 4f) of the $Pt/Co_3O_4(111)$ model catalyst after preparation. **b** LEED pattern (138 eV) and XPS (Co 2p) of the $Co_3O_4(111)$ film after transfer into the electrochemical environment and vice versa (pH 10, 0.1 M K/H_3PO_4 buffer); XPS (Pt 4f) of the $Pt/Co_3O_4(111)$ model catalyst after transfer into the electrochemical cell and back (pH 10, 0.1 M K/H_3PO_4 buffer). XPS spectra were recorded with a monochromated Al Kα source (1486.6 eV). Reproduced with permission from Ref. [41], Copyright 2018, Nature Publishing Group
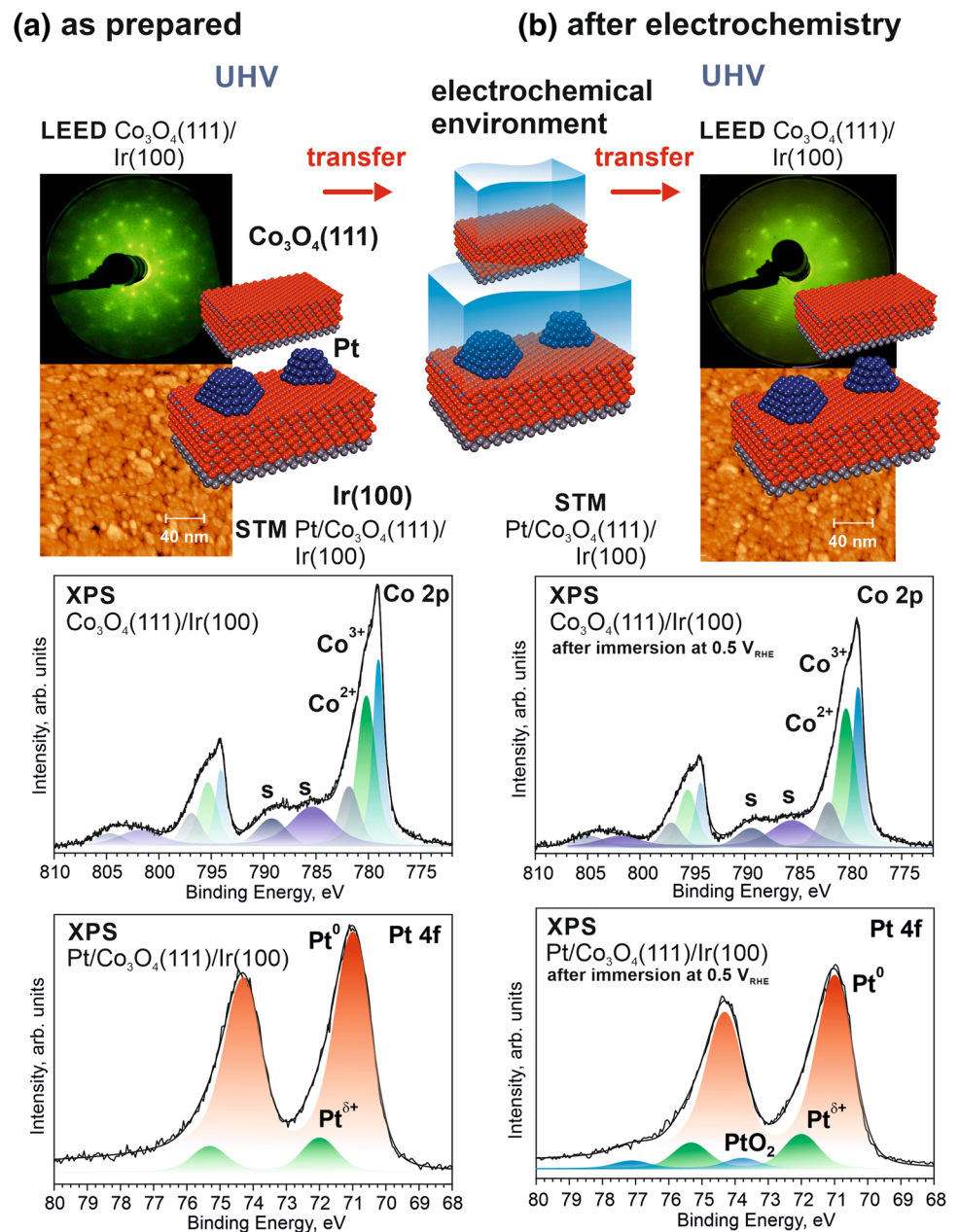
compared to the initial spectrum after UHV preparation. In the O 1s spectrum the intensity of the contributions from hydroxyl groups/phosphate, chemisorbed and physisorbed water increases after emersion due to water adsorption and dissociation [36]. The analysis of the film thickness by ex-situ emersion XPS did not show perceptible changes below 1.2 V_{RHE}. Only at potentials above 1.2 V the film thickness increases slightly (5%), most likely due to formation of CoOOH at the surface [36]. When leaving the stability window towards reducing conditions, the Co 2p spectra drastically change at -0.2 V_{RHE}, indicating formation of Co^0 and $Co(OH)_2$. Additionally the Ir signal in the Ir 4f spectrum increased indicating dissolution and restructuring of

the $Co_3O_4(111)$ film [36]. The results demonstrate that it is possible to preserve the atomic structure of the $Co_3O_4(111)$, but it is mandatory to maintain the sample in a well-defined stability window under all conditions [36, 37].

The stability of $Pt/Co_3O_4(111)$ supported NPs under reaction conditions was investigated by STM [41], ex-situ [40] and ex-situ emersion XPS [36, 41] and EC-IRRAS [41]. STM images (Fig. 4) before and after exposure to electrochemical conditions (0.3–1.1 V_{RHE}, phosphate buffer) show that the morphology of the catalysts does not change in the course of the experiment. By probing the surface with CO and performing several CO oxidation cycles, we demonstrated that the adsorption sites do not change over several

cycles. While the Pt 4f spectra after preparation show features of metallic Pt^0 at 70.9 eV and partially oxidized $Pt^{\delta+}$ at 72.0 eV after immersion at 0.5 V_{RHE} an additional feature appears at 73.8 eV which is assigned to Pt^{4+} (see Fig. 4).

5 Redox Behavior of Pt/Co$_3$O$_4$(111)

In the next step, we investigated the redox behavior of Pt NPs on Co$_3$O$_4$(111) both in UHV and in electrochemical environment [36, 38]. Figure 5a shows the Pt 4f spectra after Pt deposition onto Co$_3$O$_4$(111) at 300 K measured with synchrotron radiation photoemission spectroscopy (SR-PES) in UHV. At very low coverage, only a single feature at 72.3 eV is observable, which we assigned to partially oxidized $Pt^{\delta+}$. Note that the charge of this partially oxidized $Pt^{\delta+}$ was determined to be ~ 0.1 [68]. With increasing Pt coverage, a second feature appears at 71.3 eV, which becomes dominant at higher Pt coverage. We assign this component to metallic Pt^0. Here the partially oxidized species is most likely located

at the interface between the metallic Pt particle and the oxide support. When increasing the temperature (Fig. 5b), the $Pt^{\delta+}$ species at 72.3 eV vanishes at temperatures between 400 and 450 K due to reduction of $Pt^{\delta+}$. Above 450 K, the Pt^0 signal decreases mainly because of sintering of the NPs [38].

By ex-situ emersion XPS, we addressed the redox behavior under electrochemical conditions [36]. Figure 6 shows the Pt 4f spectra of Pt/Co$_3$O$_4$(111) with a particle size of ~ 2.5 nm after preparation. The sample was emersed at potentials between 0.5 and 1.4 V_{RHE}, and finally after returning to 0.5 V_{RHE}. The spectra of initially prepared Pt/Co$_3$O$_4$(111) contain features at 70.9 eV for Pt^0 and at 72.0 eV for $Pt^{\delta+}$ and the cobalt oxide (data not shown) is partially reduced due to metal support interaction. After emersion at 0.5 V_{RHE}, an additional species appears at 73.8 eV, which we assign to interfacial Pt^{4+}. The cobalt oxide becomes reoxidized (data not shown), which we assign to dissociation at $Pt^{\delta+}$ sites and oxygen spillover to the support [36]. The intensity of the Pt^{4+} feature is moderately low between 0.5 and 1.0 V_{RHE}. At 1.0 V_{RHE} the feature at

Fig. 5 SR-PES data in UHV of the Pt 4f region measured for Pt deposition on Co$_3$O$_4$(111) and after subsequent annealing. **a** Pt 4f spectra taken at different Pt loadings; **b** Pt 4f spectra taken after annealing of Pt/Co$_3$O$_4$(111) (Pt loading 2.0 ML) to temperatures between 300 and 850 K. The contributions from $Pt^{\delta+}$ and Pt^0 are marked green and red, respectively. All spectra were acquired with a photon energy of 180 eV. Reproduced with permission from Ref. [38], Copyright 2018, American Chemical Society (Color figure online)
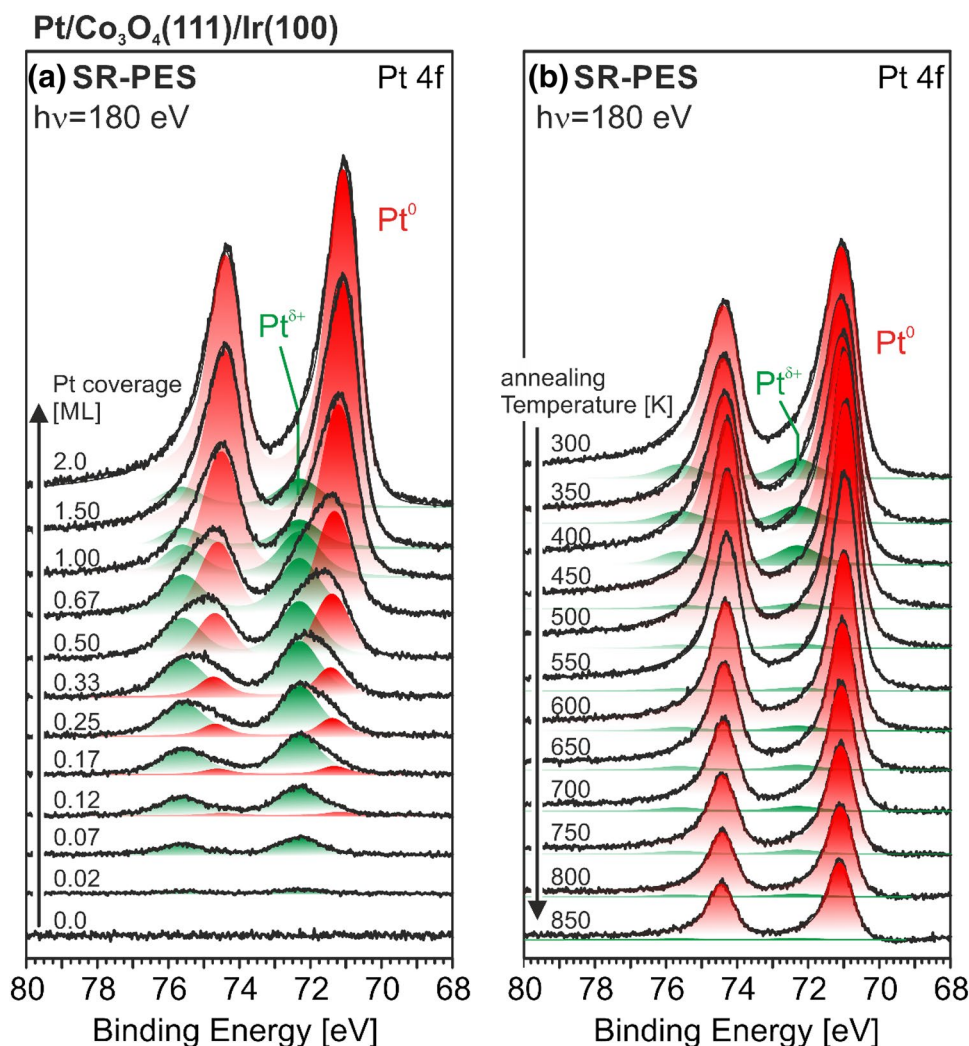
Fig. 6 Pt 4f (**a**) spectra were obtained from the Pt/Co$_3$O$_4$(111)/Ir(100) film following the electrochemical treatment at different electrode potentials. The evolution of the integrated Pt 4f intensities associated with Pt^0 (**b**), Pt$^{\delta+}$ + Pt^{2+} (**c**), and Pt^{4+} (**d**) species is shown as a function of electrode potential. The Pt 4f spectra in (**a**) were obtained with a monochromated Al Kα X-ray source (1486.6 eV). Red circles and squares mark the data obtained before and after the electrochemical treatment and returning to 0.5 V$_{RHE}$, respectively. Reproduced with permission from Ref. [36], Copyright 2018, American Chemical Society (Color figure online)
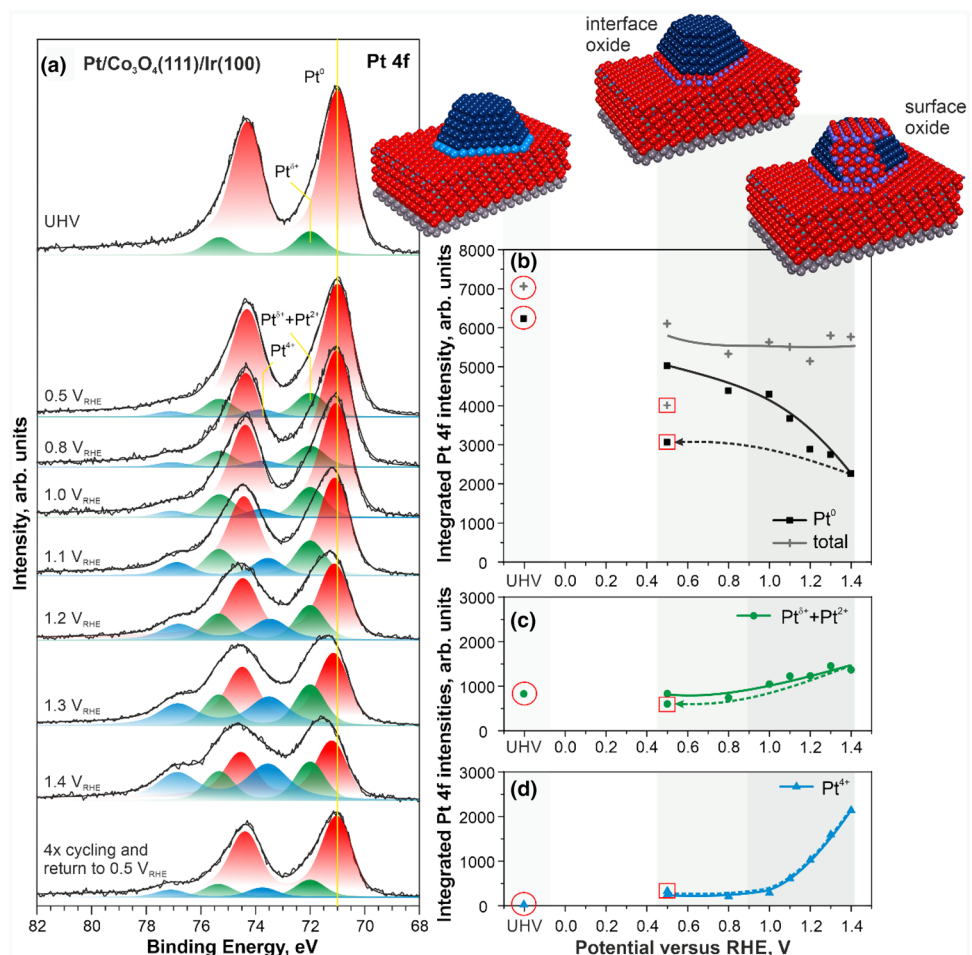

72.0 eV increases and we assign this to formation of surface PtO [36]. Note that the peak positions of Pt$^{\delta+}$, PtOH, and Pt^{2+} are overlapping. At 1.1 V$_{RHE}$ and above, the feature of Pt^{4+} increases due to the formation of surface PtO$_2$. While the onsets for the surface oxide formation are in good agreement with carbon supported Pt NPs and Pt surfaces, we reported the formation of interfacial Pt-oxide for the first time at potentials as low as 0.5 V$_{RHE}$ [36]. We attribute the appearance of the Pt-oxide at such low potential to the electronic metal support interaction and the stabilization of oxides at the oxide NP-interface [69]. Kinetically, formation of the oxide phase may be facilitated by reverse oxygen spillover and/or dissociation of OH adsorbed on Pt$^{\delta+}$. No substantial changes are observed in the total intensity of the Pt4f spectra, indicating that the sample is stable with respect to sintering in this potential region. While Co^{3+} ions in Pt/Co$_3$O$_4$(111) are partially reduced upon Pt deposition, the surface Co is reoxidized upon immersion at 0.5 V$_{RHE}$. Most likely, this is due to water dissociation at Pt$^{\delta+}$ and oxygen spillover. When we applied 4 redox cycles between 0.3 and 1.4 V$_{RHE}$ and returned to 0.5 V$_{RHE}$, the Pt$^{\delta+}$ and Pt^{4+} intensities were found to be comparable to the Pt$^{\delta+}$ and Pt^{4+}

intensities measured initially at 0.5 V$_{RHE}$. The intensity of Pt^0 is only partially recovered, indicating minor Pt dissolution [36]. For details on Pt dissolution, we refer to studies by Cherevko et al. [70].

6 CO Oxidation on Pt/Co$_3$O$_4$(111) and Particle Size Effects

We investigated the Pt/Co$_3$O$_4$(111) model electrocatalysts under reaction conditions using CO oxidation as the model reaction. This reaction is a very simple oxidation reaction and extremely well studied both in UHV [71, 72] as well as in electrochemistry [73–79]. Applying in-situ IR spectroscopy, adsorbed CO can serve as a probe for different adsorption sites [80]. Figure 7a shows the stepwise adsorption of CO on Pt/Co$_3$O$_4$(111) with conventional Pt NPs (~ 2.5 nm, 400 atoms per particle) in UHV. The spectrum shows the typical CO on-top band (CO$_t$) between 2075 and 2100 cm^{-1}. The band shifts to higher wavenumbers with increasing CO coverage, mainly because of defects and dipole interaction [80]. While CO adsorbs first at low coordinated adsorption

CO adsorption on Pt/Co$_3$O$_4$(111)
(a) in ultrahigh vacuum   **(b) under electrochemical conditions**
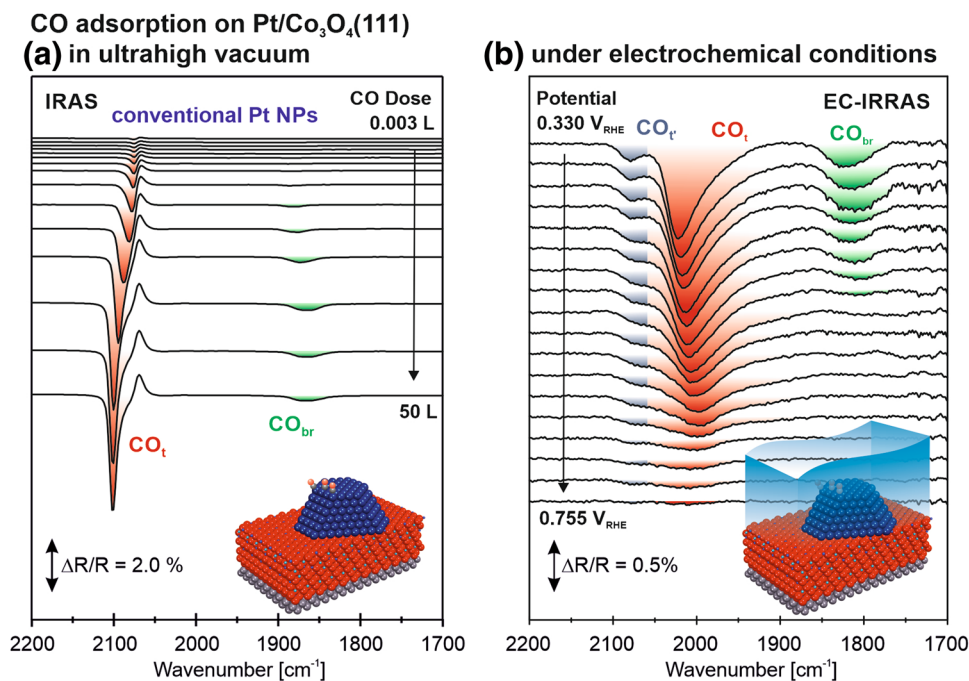
sites, it probes also the facet sites with increasing coverage while, in addition, also the dipole coupling intensifies. Both effects result in a blue shift. At 1860 cm^{-1} a band is observable, which is attributed to bridge bonded CO (CO$_b$). Using identical samples, both in UHV (Fig. 7a) and in electrochemical environment (Fig. 7b), we can directly compare the spectra in the different environments. In electrochemical environment, we adsorbed CO at + 0.33 V$_{RHE}$ and subsequently oxidized CO by increasing the potential stepwise to + 0.76 V$_{RHE}$. The bands at 2020 and 1825 cm^{-1} we assign to CO$_t$ and CO$_b$, respectively. The CO on-top band shifts to lower wavenumbers with increasing potential. While the Stark effect induces a blue shift with increasing potential, this effect is overcompensated by the decreasing dipole coupling due to the oxidation of CO, resulting in a red shift. Additionally, anion adsorption might also contribute to the redshift due to strengthening of the CO back donation. At 2080 cm^{-1}, there is an additional band the nature of which is still under debate. While we tentatively assigned this to a carbonyl like Pt species, results by Christopher et al. [81, 82] might suggest an assignment to strongly bound CO on oxidized Pt. This interpretation would be in agreement with the results obtained by ex-situ emersion XPS, where we found an additional Pt^{4+} species at low electrode potentials [36]. A direct comparison of the results obtained in UHV and in the electrochemical environment show that the bands in electrochemical environment are shifted to lower wavenumbers and exhibit a distinct broadening. This broadening is much more pronounced on Pt NPs than on Pt(111) (see Fig. 8). The redshift arises from the polarizability of the electrolyte, from lower CO coverages at higher buffer concentrations and from

the Stark effect. The broadening we assign to coupling with the electrolyte and to the inhomogeneity of the adsorption sites. Most likely, however, the broadening mainly arises from the inhomogeneity of the electric field, which gives rise to different Stark shifts at different positions on the NP.

Particle size effects are a well-known phenomenon both in heterogeneous [83, 84] and in electrocatalysis [85, 86]. UHV preparation allows us to vary the particle size in a controlled manner and to study the particle size effects of oxide supported Pt NPs, both in electrochemical environment and under UHV conditions [40]. In Fig. 8 we show spectra of adsorbed CO on Pt NPs with diameters from the subnanometer to the nanometer regime as well as on Pt(111). The comparison of the IR spectra of CO adsorption on Pt(111) in electrochemical environment and in UHV shows clear differences in the CO$_t$/CO$_b$ ratio. Note that the intensity ratio of the on-top and bridge bonded CO peak does not reflect the actual coverage due to dipole coupling effects and differences in the dynamic dipole moments. While XPS data on Pt(111) show that the ratio between CO on-top and bridge bonded CO in UHV is ~ 1:1 at saturation coverage [87], the intensity of CO$_b$ is 5 times lower than that of CO$_t$. In EC-IRRAS the ratio between CO on-top and bridge bonded CO on Pt(111) is ~ 1 indicating that CO adsorbs preferentially in bridge bonded adsorption geometry in the electrochemical environment. We assume that coadsorption of anions (phosphate, OH$^-$) suppresses CO adsorption in on-top position [40]. On the nanoparticles, the preferential CO binding motive changes from bridging to on-top and with decreasing particle size CO$_b$ is further suppressed. On very small NPs (0.27 ML Pt) no
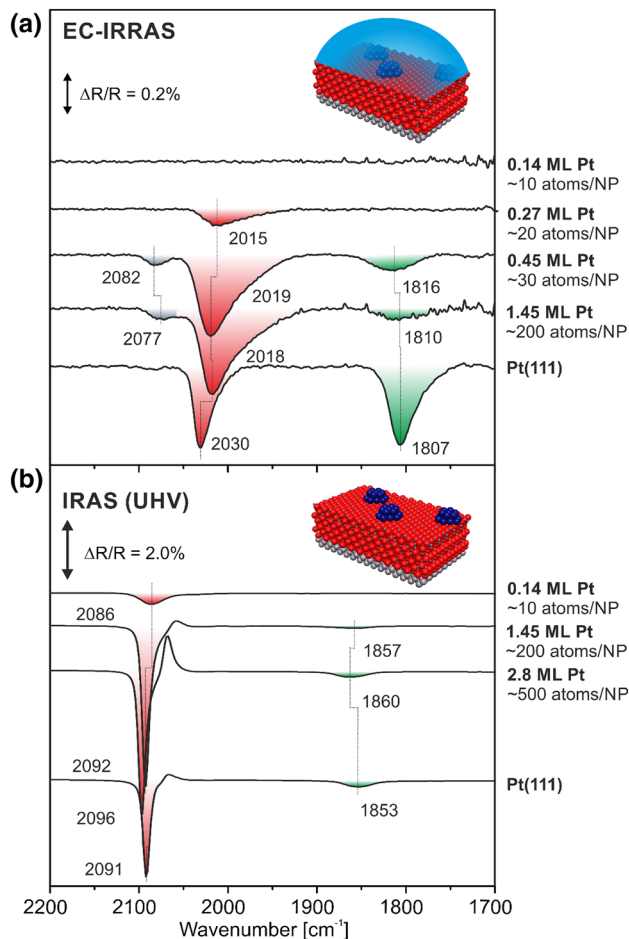
Fig. 8 Comparison of the IR spectra of adsorbed CO on Pt/Co$_3$O$_4$(111) with varying particle sizes recorded **a** in the electrochemical environment (1 M phosphate buffer, pH 10) and **b** in UHV environment. The EC-IRRAS spectra are recorded at a potential of 0.33 V$_{RHE}$ and referenced against 0.805 V$_{RHE}$. The IRRAS spectra in UHV are recorded after exposure to 49 L CO. Reproduced from Ref. [40] with permission from the PCCP Owner Society

Fig. 9 CVs taken during CO stripping from Pt NPs on Co$_3$O$_4$/Ir(100); **a** Pt(111) reference, **b** 2.8 ML Pt/Co$_3$O$_4$(111), **c** 1.4 ML Pt/Co$_3$O$_4$(111), **d** 0.45 ML Pt/Co$_3$O$_4$(111); **e** 0.27 ML Pt/Co$_3$O$_4$(111), **f** 0.14 ML Pt/Co$_3$O$_4$(111), and **g** Co$_3$O$_4$(111). All CVs were taken in 0.1 M phosphate buffer at pH 10 with a scan rate of 50 mV s^{-1}. Reproduced from Ref. [40] with permission from the PCCP Owner Society

bridge bonded CO was detected. We assign this dependence to an increased fraction of low coordinated adsorption sites binding CO more strongly and, therefore, leading to a strong preference for CO$_t$. An increasing fraction of low coordinated adsorption sites is also indicated by the red-shift of the CO on-top signal for small Pt NPs [40]. Note that the CO$_t$ red-shifts with decreasing coordination number [25]. Finally, at very low Pt coverages (0.14 ML) no CO adsorption is detected, even though EC-IRRAS is highly sensitive for CO at low coverage (detection limit below 1% of a monolayer). We attribute this observation to electronic metal support interactions (EMSI), which we discuss in more detail in the following chapter. In UHV, the CO$_t$/CO$_b$ ratio also decreases with decreasing Pt particle size and the CO$_t$ shifts to lower wavenumbers. This is
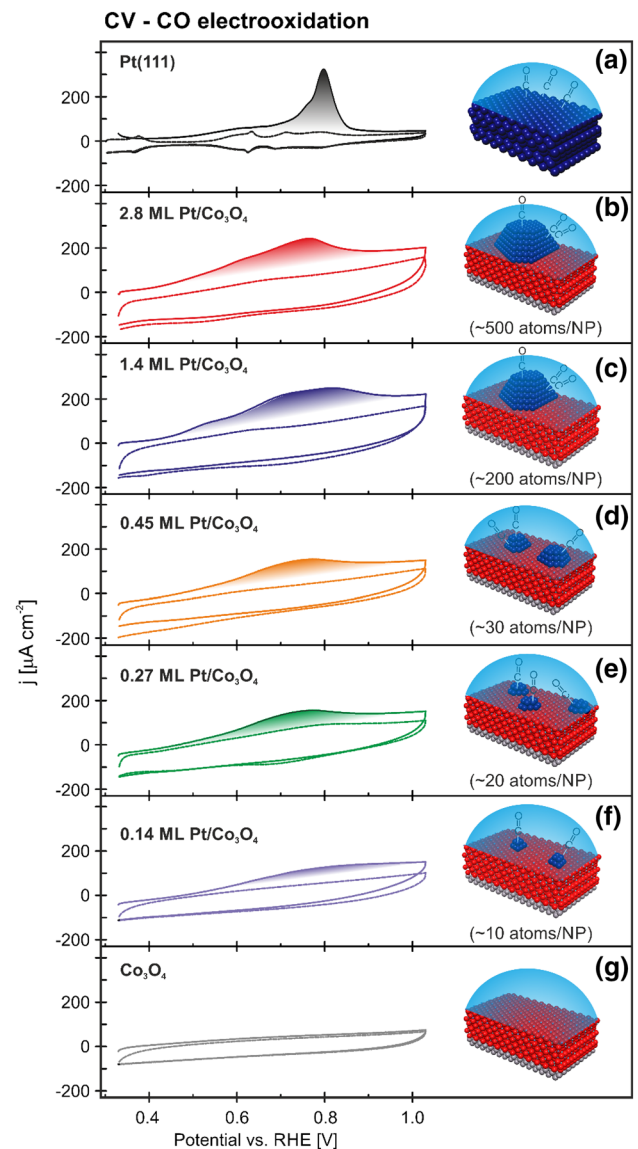
in analogy to the behavior observed under electrochemical conditions.

CVs of the CO stripping experiment are shown in Fig. 9 for Pt(111) and Pt NPs on Co$_3$O$_4$(111) with particle sizes from 2.8 to 0.14 ML [40]. The first cycle for Pt(111) shows a peak at 0.79 V$_{RHE}$, which corresponds to CO adsorption on (111) facets. Additionally there are shoulders at 0.76 and 0.60 V$_{RHE}$, which result from CO adsorption at low coordinated Pt sites. In the hydrogen region, no peak is observable due to blocking by preadsorbed CO. The second CV cycle

shows the typical features of Pt(111) in phosphate buffer at pH 10 [88, 89]. All Pt/Co$_3$O$_4$(111) samples show resistive and capacitive backgrounds due to the semiconducting nature of Co$_3$O$_4$ [90]. The CO oxidation peaks decrease with decreasing particle size and the CO oxidation peaks of the particles are much broader as compared to Pt(111) with a distinct shoulder towards lower potentials. This is induced, on the one hand, by a high number of low coordinated adsorption sites and, on the other hand, by a supporting effect of the oxide, which acts as OH donor through reverse oxygen spillover effects [40].

7 Metal Support Interaction

Metal support interactions play a major role in oxide-supported catalysts [5, 91]. To address the metal support interaction we investigated the CO adsorption on freshly prepared Pt/Co$_3$O$_4$(111) in UHV at 115 K [38]. At this temperature, weakly adsorbed CO is detected as well. In Fig. 10
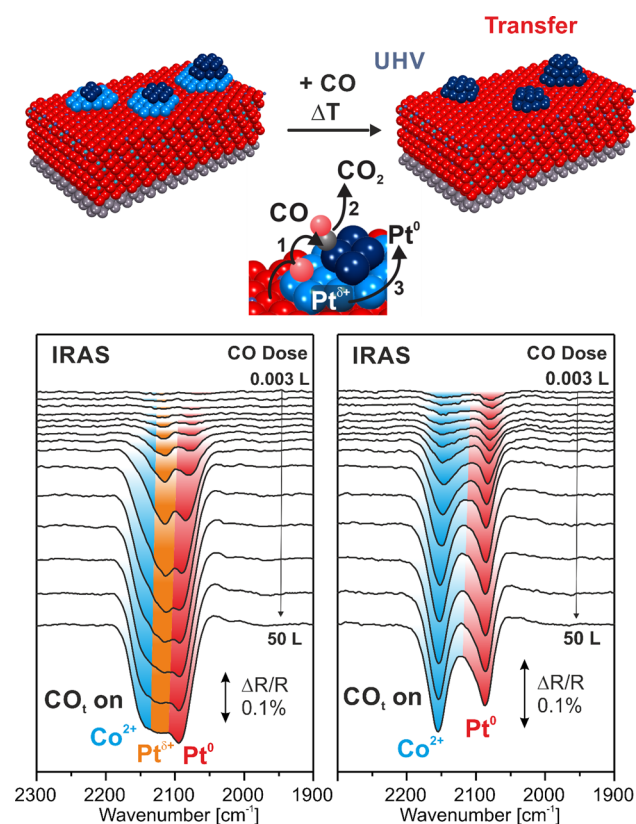

Fig. 10 IRAS spectra acquired at 115 K after saturation of the Pt/Co$_3$O$_4$(111) with CO before (left) and after (right) annealing to 550 K. The bands highlighted in red, orange, and cyan are assigned to CO adsorbed on metallic Pt^0, partially oxidized Pt$^{\delta+}$, and the Co$_3$O$_4$ support, respectively. The background was taken immediately before CO dosage. Adapted with permission from Ref. [41], Copyright 2018, Nature Publishing Group (Color figure online)

(left), we show the corresponding spectra and we identify three different CO bands. CO adsorption on metallic Pt^0, partially oxidized Pt$^{\delta+}$, and Co$_3$O$_4$(111) give rise to bands at 2090, 2115, 2150 cm^{-1}, respectively. After annealing to 550 K, the spectrum changes dramatically as shown in Fig. 10 (right). The CO$_t$ signal from metallic Pt^0 shifts to the blue and sharpens due to particle sintering and formation of well-shaped particles. The most dramatic difference is, however, seen in the band from CO adsorbed on Pt$^{\delta+}$, which vanishes completely after annealing. This observation indicates that Pt$^{\delta+}$ is fully reduced, an observation which is also confirmed by SR-PES measurements (Fig. 5). The TPD spectrum measured after the first set of IR spectra shows CO$_2$ formation. Here the oxide support acts as an oxygen source either via reverse oxygen spill-over or via reaction across the NP/oxide boundary. In the second TPD measured after the second set of IR spectra, no further CO$_2$ is formed for Pt loadings smaller than 1.36 ML Pt. This demonstrates that all oxygen available from the oxide reservoir has been consumed [38].

The question arises, if similar reaction mechanisms also exist in the electrochemical environment. CO adsorbs weakly on Pt$^{\delta+}$, which implies that such sites cannot be probed in EC-IRRAS experiments at room temperature. We address this question using an indirect approach [38]. Several cycles of CO oxidation were measured, as shown in Fig. 11a. For the smallest NPs (0.36 ML) only a single broad feature is observable at 1993 cm^{-1} that initially does not show any potential dependent shift. With increasing cycle number, the spectra show a blue shift, the intensity increases drastically, and the CO$_t$ band shows a redshift with increasing potential. Our findings suggest that Pt$^{\delta+}$ is reduced to Pt^0 and CO probes these metallic adsorption sites at room temperature. The blueshift and the potential dependent shift arise from the enhanced dipole coupling with increasing size of the metallic aggregate. At larger Pt coverage the CO$_t$ band also increases, but the effect is less pronounced. We plotted the relative band intensities of the CO bands versus the potential cycle in Fig. 11b for the different particle sizes and for Pt(111) as a reference. While the band intensity does not change with cycling for Pt(111), the band intensity increases for the Pt nanoparticles, especially for the small ones. Note that we observed the largest fraction of Pt$^{\delta+}$ being formed at the smallest Pt coverages. We propose that this Pt$^{\delta+}$ is reduced during CO oxidation as a result of oxygen reverse spillover from the oxide support to the supported NPs. Similar effects are commonly observed in heterogeneous catalysis and have been investigated in model studies in UHV in great detail [5, 6]. From the results, we conclude that a similar reaction mechanism is also possible in the electrochemical environment. Finally, we compare the Pt^0 signal obtained from SR-PES with the CO$_t$ band intensity from EC-IRRAS for different particle sizes (Fig. 12). At
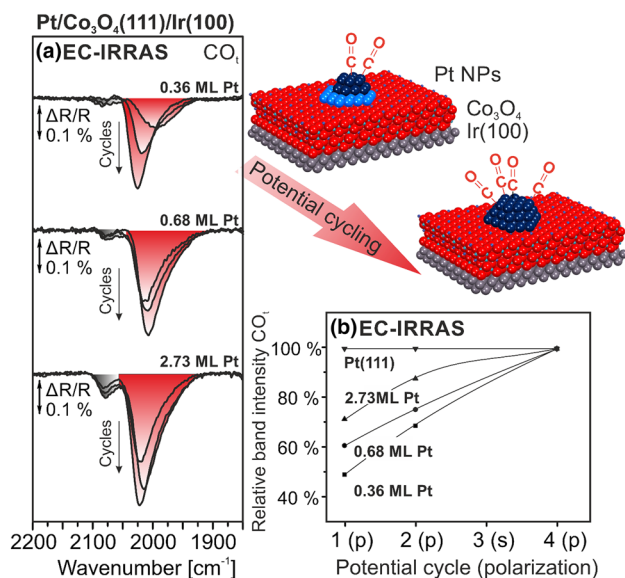
Fig. 11 a Comparison of the EC-IRRAS data (pH 10, 1 M phosphate buffer) of the CO stretching frequency region for different CO adsorption and electrooxidation cycles on Pt/Co_3O_4(111) model catalysts with different Pt NP sizes; **b** comparison of the development of the band intensity in the CO stretching frequency region as a function of the Pt NP size, compared to the data obtained from clean Pt(111). All spectra were recorded at 0.33 V_{RHE} and were referenced to the spectrum at 0.805 V_{RHE}. Top right: schematic sketch of the model system with Ir(111) (silver), Co_3O_4(111) (red), Pt^0(dark blue), and $Pt^{\delta+}$ (light blue). Reproduced with permission from Ref. [38], Copyright 2018, American Chemical Society (Color figure online)
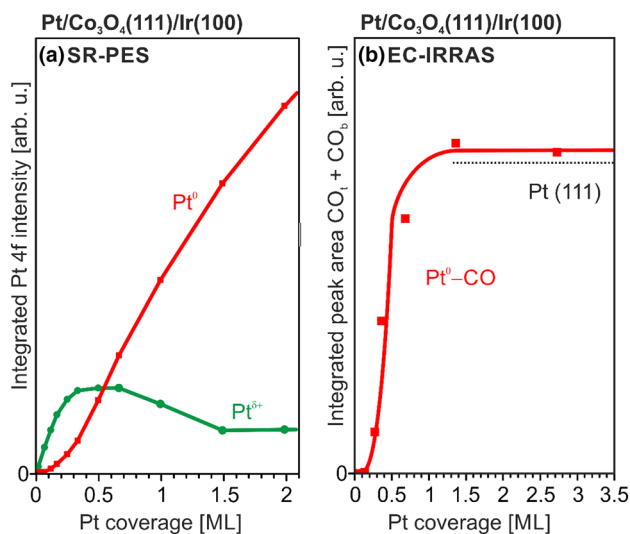

Fig. 12 a Intensity of the $Pt^{\delta+}$ and Pt^0 component derived from SR-PES experiment as a function of the Pt loading; **b** intensity of the on-top CO stretching band derived from EC-IRRAS experiments as a function of the Pt loading. Reproduced with permission from Ref. [38], Copyright 2018, American Chemical Society

high Pt coverages, Pt^0 is the dominant Pt species in SR-PES. At Pt coverages ≤ 1 ML the situation changes drastically. The $Pt^{\delta+}$ signal increases and becomes the dominant species at coverages of 0.5 ML Pt. At Pt coverages below 0.1 ML, only $Pt^{\delta+}$ is present. The peak intensities in EC-IRRAS show a similar dependence as a function of the Pt loading. The CO band intensity decreases rapidly below a coverage of 1 ML Pt and at very low Pt coverages of ~0.1 ML, we observed no CO signal at all [38]. From this comparison, we conclude that very similar metal support interactions are present both in UHV and in electrochemical environment. This metal support interaction then enables a new reaction mechanism, which involves oxygen reverse spillover and the subsequent reduction of $Pt^{\delta+}$.

8 Summary and Future Perspective

This perspective summarizes our first series of studies investigating complex atomically defined model electrocatalysts based on ordered oxide films. We prepared these oxide based model electrocatalysts by surface science methods in UHV and studied the samples in UHV and under electrochemical conditions. Specifically, our model electrocatalysts consist of Pt NP which are prepared by physical vapor deposition on a Co_3O_4(111) thin film on Ir(100). We varied the size of the Pt NPs between the range of sub-nanometer particles and the range of more conventional nanoparticles with diameters of a few nanometers. We investigated the stability of the Co_3O_4(111) and Pt/Co_3O_4(111) model electrodes, studied the redox behavior of the Pt/Co_3O_4(111) electrocatalyst, and used the CO oxidation as model reaction. In our studies, we used a variety of surface science and electrochemical methods such as IRAS, SR-PES, TPD, STM, EC-IRRAS, ex-situ emersion XPS, and CV and online ICPMS. From the results, we conclude the following:

1. *Transfer and stability* It is possible to prepare atomically defined oxide-based model catalysts in UHV and transfer these model electrocatalysts into the electrolyte, while keeping their surface clean and preserving the atomic structure in the electrochemical environment. For Pt/Co_3O_4, the stability window is between 0.3 and 1.1 V_{RHE} in phosphate buffer at pH 10. Within this stability window, cobalt dissolution from the Co_3O_4(111) support is below the detection limit (< 0.2 ML h^{-1}) and the surface structure of the support is preserved.

2. *Redox behavior of Pt/Co_3O_4(111)* Charge transfer effects play an important role for the adsorption and reaction behavior of Pt/Co_3O_4(111) electrocatalysts. These charge transfer effects induce the formation of (partially) oxidized Pt species at the metal/metal oxide interface. In UHV interfacial $Pt^{\delta+}$ is formed, which is stable in the

electrochemical environment at potential as low as 0.5 V_{RHE}. Here a small fraction of interfacial Pt^{4+} is formed additionally. By increasing the potential to 1.1 V_{RHE} and above, Pt^{2+} and Pt^{4+} surface species are formed, which is in accordance with classical behavior known for Pt NPs on a carbon support.

3. *Particle size effects* Pt NPs on $Co_3O_4(111)$ show distinct particle size effects for CO adsorption both in UHV and in the electrochemical environment. While CO adsorbs on conventional NPs both in on-top and bridge bonded geometry, formation of bridge bonded CO is fully suppressed on subnanometer particles due to the domination of low coordinated adsorption sites.

4. *Metal support interactions and spillover effects* In UHV adsorbed CO is oxidized to CO_2 on freshly prepared Pt/$Co_3O_4(111)$ by a reverse oxygen spillover effect, while partially oxidized $Pt^{\delta+}$ is reduced. We observe a quite similar reaction also in electrochemical environment. This observation demonstrates that on oxide supported electrocatalysts a new reaction pathway is possible, which includes partially oxidized $Pt^{\delta+}$. Finally, we demonstrated that with decreasing Pt loading $Pt^{\delta+}$ becomes the dominating species. At very low Pt coverages, formation of Pt^0 is even fully suppressed. This indicates that reverse oxygen spill-over plays a major role for the reactivity of these supported NPs, especially for very small sizes.

The studies summarized in this review illustrate the potential of the experimental approach. By electrifying model catalysts made and characterized under surface science conditions, a broad range of complex yet atomically defined model electrodes becomes available. First of all the approach enables to use a variety of different well-ordered oxide supports. Further, we envision studying the interaction of different noble metals with these oxide supports. The use of alloy particles will further increase the complexity and will add additional functionalities to the systems. Additional functionalities are essential to catalyze complex reactions efficiently. By transferring the approach to these more complex reactions we envision that this will help finally to close the materials gap between electrochemical surface science with single crystal surfaces and applied electrocatalysis with complex nanostructured materials.

References

1. Kuhlenbeck H, Shaikhutdinov S, Freund H-J (2013) Chem Rev 113:3986–4034
2. Farmer JA, Campbell CT (2010) Science 329:933–936
3. Schauermann S, Hoffmann J, Johanek V, Hartmann J, Libuda J, Freund H-J (2002) Angew Chem Int Ed 41:2532
4. Rodriguez JA, Ma S, Liu P, Hrbek J, Evans J, Perez M (2007) Science 318:1757–1760
5. Lykhach Y, Kozlov SM, Skala T, Tovt A, Stetsovych V, Tsud N, Dvorak F, Johanek V, Neitzel A, Myslivecek J, Fabris S, Matolín V, Neyman KM, Libuda J (2016) Nat Mater 15:284–288
6. Vayssilov GN, Lykhach Y, Migani A, Staudt T, Petrova GP, Tsud N, Skála T, Bruix A, Illas F, Prince KC, Matolín V, Neyman KM, Libuda J (2011) Nat Mater 10:310–315
7. Freund H-J, Kuhlenbeck H, Libuda J, Rupprechter G, Bäumer M, Hamann H (2001) Top Catal 15:201–209
8. Kolb DM (2001) Angew Chem Int Ed 40:1162–1181
9. Korzeniewski C, Climent V, Feliu JM (2012) In: Bard AJ, Zoski C (eds) Electroanalytical chemistry: a series of advances, vol 24. CRC Press, Boca Raton, pp 75–170
10. Weaver MJ, Gao XP (1993) Annu Rev Phys Chem 44:459–494
11. Kolb DM (2011) J Solid State Electrochem 15:1391–1399
12. Koper MT (2011) Nanoscale 3:2054–2073
13. Clavilier J, Faure R, Guinet G, Durand R (1979) J Electroanal Chem Interfacial Electrochem 107:205–209
14. Magnussen OM, Groß A (2019) J Am Chem Soc 141:4777–4790
15. Xu C, Shen PK (2004). Chem Commun:2238–2239.
16. Xu C, Shen PK (2005) J Power Sources 142:27–29
17. Xu C, Zeng R, Shen PK, Wei Z (2005) Electrochim Acta 51:1031–1035
18. Xu C, Shen PK, Ji X, Zeng R, Liu Y (2005) Electrochem Commun 7:1305–1308
19. Shen PK, Xu C (2006) Electrochem Commun 8:184–188
20. Xu C (2007) Shen Pk, Liu Y. J Power Sources 164:527–531
21. Xu C, Tian Z, Shen P, Jiang SP (2008) Electrochim Acta 53:2610–2618
22. Antolini E, Gonzalez ER (2010) J Power Sources 195:3431–3450
23. Lykhach Y, Bruix A, Fabris S, Potin V, Matolínová I, Matolín V, Libuda J, Neyman KM (2017) Cat Sci Technol 7:4315–4345
24. Lykhach Y, Brummel O, Bruix A, Fabris S, Matolínová I, Matolín V, Neyman KM, Libuda J (2018) In: Wandelt K (ed) Encyclopedia of interfacial chemistry. Elsevier, Oxford, pp 189–201
25. Brummel O, Waidhas F, Faisal F, Fiala R, Vorokhta M, Khalakhan I, Dubau M, Figueroba A, Kovács G, Aleksandrov HA, Vayssilov GN, Kozlov SM, Neyman KM, Matolín V, Libuda J (2016) J Phys Chem C 120:19723–19736
26. Hoster HE, Gasteiger HA (2010) In: Handbook of fuel cells. Wiley, Hoboken
27. Mercer MP, Hoster HE (2016) Nano Energy 29:394–413
28. Kolb DM (1987) Z Phys Chem 154:179
29. Brimaud S, Engstfeld AK, Alves OB, Hoster HE, Behm RJ (2014) Top Catal 57:222–235

30. Bergbreiter A, Alves OB, Hoster HE (2010) ChemPhysChem 11:1505–1512
31. Stamenković VR, Arenz M, Lucas CA, Gallagher ME, Ross PN, Marković NM (2003) J Am Chem Soc 125:2736–2745
32. Schnaidt J, Beckord S, Engstfeld AK, Klein J, Brimaud S, Behm RJ (2017) Phys Chem Chem Phys 19:4166–4178
33. Müllner M, Balajka J, Schmid M, Diebold U, Mertens SFL (2017) J Phys Chem C 121:19743–19750
34. Müllner M, Riva M, Kraushofer F, Schmid M, Parkinson GS, Mertens SFL, Diebold U (2019) J Phys Chem C 123:8304–8311
35. Fester J, Makoveev A, Grumelli D, Gutzler R, Sun Z, Rodríguez-Fernández J, Kern K, Lauritsen JV (2018) Angew Chem Int Ed 57:11893–11897
36. Brummel O, Lykhach Y, Vorokhta M, Šmíd B, Stumm C, Faisal F, Skála T, Tsud N, Neitzel A, Beranová K, Prince KC, Matolín V, Libuda J (2019) J Phys Chem C 123:8746–8758
37. Faisal F, Bertram M, Stumm C, Cherevko S, Geiger S, Kasian O, Lykhach Y, Lytken O, Mayrhofer KJJ, Brummel O, Libuda J (2018) J Phys Chem C 122:7236–7248
38. Faisal F, Bertram M, Stumm C, Wähler T, Schuster R, Lykhach Y, Neitzel A, Skála T, Tsud N, Beranová K, Prince KC, Matolín V, Brummel O, Libuda J (2018) J Phys Chem C 122:20787–20799
39. Faisal F, Bertram M, Stumm C, Waidhas F, Brummel O, Libuda J (2018) Rev Sci Instrum 89:114101
40. Faisal F, Stumm C, Bertram M, Wähler T, Schuster R, Xiang F, Lytken O, Katsounaros I, Mayrhofer KJJ, Schneider MA, Brummel O, Libuda J (2018) Phys Chem Chem Phys 20:23702–23716
41. Faisal F, Stumm C, Bertram M, Waidhas F, Lykhach Y, Cherevko S, Xiang F, Ammon M, Vorokhta M, Šmíd B, Skala T, Tsud N, Neitzel A, Beranova K, Prince K, Geiger S, Kasian O, Wähler T, Schuster R, Schneider M, Matolin V, Mayrhofer K, Brummel O, Libuda J (2018) Nat Mater 17:592–598
42. Pajkossy T, Wandlowski T, Kolb DM (1996) J Electroanal Chem 414:209–220
43. Sonnenfeld R, Hansma PK (1986) Science 232:211–214
44. Sonnenfeld R, Schardt BC (1986) Appl Phys Lett 49:1172–1174
45. Manne S, Hansma PK, Massie J, Elings VB, Gewirth AA (1991) Science 251:183–186
46. Favaro M, Jeong B, Ross PN, Yano J, Hussain Z, Liu Z, Crumlin EJ (2016) Nat Commun 7:12695
47. Favaro M, Abdi FF, Crumlin EJ, Liu Z, van de Krol R, Starr DE (2019) Surfaces 2:78–99
48. Baltruschat H (2004) J Am Soc Mass Spectrom 15:1693–1706
49. Grimaud A, Diaz-Morales O, Han BH, Hong WT, Lee YL, Giordano L, Stoerzinger KA, Koper MTM, Shao-Horn Y (2017) Nat Chem 9:457–465
50. Khanipour P, Löffler M, Reichert AM, Haase FT, Mayrhofer KJJ, Katsounaros I (2019) Angew Chem Int Ed 58:7273–7277
51. Braunschweig B, Mukherjee P, Dlott DD, Wieckowski A (2010) J Am Chem Soc 132:14036–14038
52. Bewick A, Kunimatsu K, Pons BS, Russell JW (1984) J Electroanal Chem Interfacial Electrochem 160:47–61
53. Bewick A, Kunimatsu K (1980) Surf Sci 101:131–138
54. Iwasita T, Nart FC (1997) Prog Surf Sci 55:271–340
55. Soriaga MP (1992) Prog Surf Sci 39:325–443
56. Parsons R (1989) In: Compton RG (ed) Comprehensive chemical kinetics, vol 29. Elsevier, Amsterdam, pp 105–127
57. Hans-Joachim F, Helmut K, Volker S (1996) Rep Prog Phys 59:283
58. Liang Y, Li Y, Wang H, Zhou J, Wang J, Regier T, Dai H (2011) Nat Mater 10:780
59. Jiao F, Frei H (2009) Angew Chem Int Ed 48:1841–1844
60. Sun S, Sun L, Xi S, Du Y, Prathap MUA, Wang Z, Zhang Q, Fisher A, Xu ZJ (2017) Electrochim Acta 228:183–194
61. Reikowski F, Maroun F, Pacheco I, Wiegmann T, Allongue P, Stettner J, Magnussen OM (2019) ACS Catal 9:3811–3821
62. Heinz K, Hammer L (2013) J Phys Condens Matter 25:173001
63. Meyer W, Biedermann K, Gubo M, Hammer L, Heinz K (2008) J Phys: Condens Matter 20:265011–265017
64. Ferstl P, Mehl S, Arman MA, Schuler M, Toghan A, Laszlo B, Lykhach Y, Brummel O, Lundgren E, Knudsen J, Hammer L, Schneider MA, Libuda J (2015) J Phys Chem C 119:16688–16699
65. Chivot J, Mendoza L, Mansour C, Pauporté T, Cassir M (2008) Corros Sci 50:62–69
66. Schuppert AK, Topalov AA, Katsounaros I, Klemm SO, Mayrhofer KJJ (2012) J Electrochem Soc 159:F670–F675
67. Klemm SO, Topalov AA, Laska CA, Mayrhofer KJJ (2011) Electrochem Commun 13:1533–1535
68. Lykhach Y, Faisal F, Skála T, Neitzel A, Tsud N, Vorokhta M, Dvořák F, Beranová K, Kosto Y, Prince KC, Matolín V, Libuda J (2018) J Mater Chem A 6:23078–23086
69. Schalow T, Laurin M, Brandt B, Schauermann S, Guimond S, Kuhlenbeck H, Starr DE, Shaikhutdinov SK, Libuda J, Freund H-J (2005) Angew Chem Int Ed 44:7601–7605
70. Cherevko S, Zeradjanin AR, Keeley GP, Mayrhofer KJJ (2014) J Electrochem Soc 161:H822–H830
71. Freund H-J, Meijer G, Scheffler M, Schlögl R, Wolf M (2011) Angew Chem Int Ed 50:10064–10094
72. Engel T, Ertl G (1979) In: Eley DD, Pines H, Weez PB (eds) Advances in catalysis, vol 28. Academic Press, Amsterdam, pp 1–78
73. Beden B, Lamy C, de Tacconi NR, Arvia AJ (1990) Electrochim Acta 35:691–704
74. García G, Koper M (2011) ChemPhysChem 12:2064–2072
75. Mayrhofer KJJ, Arenz M, Blizanac BB, Stamenkovic V, Ross PN, Markovic NM (2005) Electrochim Acta 50:5144–5154
76. Koper MTM, Lai SCS, Herrero E (2008) Fuel cell catalysis. Wiley, Hoboken, pp 159–207
77. Batista EA, Iwasita T, Vielstich W (2004) J Phys Chem B 108:14216–14222
78. Farias MJS, Vidal-Iglesias FJ, Solla-Gullón J, Herrero E, Feliu JM (2014) J Electroanal Chem 716:16–22
79. Spendelow JS, Goodpaster JD, Kenis PJA, Wieckowski A (2006) J Phys Chem B 110:9545–9555
80. Hoffmann FM (1983) Surf Sci Rep 3:107–192
81. DeRita L, Dai S, Lopez-Zepeda K, Pham N, Graham GW, Pan X, Christopher P (2017) J Am Chem Soc 139:14150–14165
82. Thang HV, Pacchioni G, DeRita L, Christopher P (2018) J Catal 367:104–114
83. Sheu LL, Karpinski Z, Sachtler WMH (1989) J Phys Chem 93:4890–4894
84. Kleis J, Greeley J, Romero NA, Morozov VA, Falsig H, Larsen AH, Lu J, Mortensen JJ, Dułak M, Thygesen KS, Nørskov JK, Jacobsen KW (2011) Catal Lett 141:1067–1071
85. Hayden BE, Suchsland J-P (2008) Fuel cell catalysis. Wiley, Hoboken, pp 567–592
86. Maillard F, Pronkin S, Savinova ER (2008) Fuel cell catalysis. Wiley, Hoboken, pp 507–566
87. Kinne M, Fuhrmann T, Whelan CM, Zhu JF, Pantforder J, Probst M, Held G, Denecke R, Steinrück HP (2002) J Chem Phys 117:10852–10859
88. Gisbert R, García G, Koper MTM (2010) Electrochim Acta 55:7961–7968
89. Gisbert R, García G, Koper MTM (2011) Electrochim Acta 56:2443–2449
90. Cheng C-S, Serizawa M, Sakata H, Hirayama T (1998) Mater Chem Phys 53:225–230
91. Campbell CT (2012) Nat Chem 4:597–598

Affiliations

Olaf Brummel[1] ⬤ · **Jörg Libuda[1]** ⬤

✉ Olaf Brummel
    olaf.brummel@fau.de

[1] Interface Research and Catalysis, Erlangen Catalysis
     Resource Center, Friedrich-Alexander-Universität Erlangen-
     Nürnberg, Egerlandstrasse 3, 91058 Erlangen, Germany